

Tiny groups of galaxies remember their cosmic origins

Detection of the large-scale tidal field with galaxy multiplet alignment in the DESI Y1 spectroscopic survey

Claire Lamman ^{1*}, Daniel Eisenstein,¹ Jaime E. Barrero-Palmero ^{2,3}, Jessica Nicole Aquila ¹, Steven Ahlen ⁵, Stephen Bailey ⁴, Davide Biagioli ¹, David Brooks,¹ Todd Chapman ¹, Axel de la Macorra ⁸, Peter Doel,⁷ Simone Ferraro ⁴, Andrey Fofonov ¹⁰, Enrique Gaztañaga,^{11,12,13} Satya Gonçalo A Gentile ¹⁴, Antonio González ¹, Klaas Honscheid ^{15,16}, Cullan Howlett ¹⁸, Anthony Krenn ¹, Andre Lacerda ¹⁹, Landry Lardau ¹, Laurent Lebreton ¹⁹, Michael E. Levi ⁴, Aaron Meisner ¹, Esteban Muñoz ⁷, John Notourekas ¹, Jeffrey A. Newman ²³, Gustavo Niz ^{24,25}, Francisco Prada ²⁶, Ignacio Pérez ²⁷, Ashley J. Ross ^{15,28,17}, Graziano Rossi,²⁹ Eusebio Sanchez ³⁰, Michael Steuverell ^{31,32}, David Sprayberry,²⁰ Gregory Tarlé ³, Mariana Vargas-Magaña ⁸, Benjamin Alan Weaver ²⁰, Hsiz Zou ³³

Affiliations are listed at the end of the paper

Accepted XXX. Received YYY; in original form ZZZ

TL;DR

ABSTRACT

We explore correlations between the orientations of small galaxy groups, or “multiplets”, and the large-scale gravitational tidal field. Using data from the DESI Y1 spectroscopic survey, we find a connection between little groups of galaxies, or “multiplets”, and the largest structures in the universe. This is cool because usually stuff on small scales seems to forget the cosmic web it originated from. We find that all multiplets remember the same large-scale structure, regardless of the type of galaxies in them. This method doesn’t have the main issues that affect similar types of measurements, so it could be a useful way to measure the cosmic web.

The more we know about the cosmic web, the more we know about the stuff that shapes it: like dark energy

Key words: methods: data analysis – cosmology: observations – large-scale structure of Universe – cosmology: dark energy

BACKGROUND INFO

INTRODUCTION

As the universe evolves, gas and dust fall along massive structures of dark matter, forming galaxies and illuminating the cosmic web. The gravity of the cosmic web affects the galaxies that form along it, creating correlations between the two. For instance, a long galaxy will tend to be aligned along a cosmic strand.

tionship with the large-scale tidal field, where long axes are aligned with the tidal direction. For a pedagogical introduction to IA, see

Lamman et al. (2022) and for comprehensive reviews, see Joachimi

(2019), Slep et al. & Ishak (2020). IA can be used as a complement to other cosmological probes, such as weak lensing and redshift-space distortions (RSD). It can also be used to trace any cosmological signal, including the large-scale density field (Chisari & Dvorkin 2013). Compared to traditional two-point clustering statistics, IA can probe the amplitude and polarization of tidal fields, as is done with weak lensing. While weak lensing traces all foreground matter, IA only traces matter in the background. However, the effect is subtle and requires large samples

E-mail: claire.lamman@cfa.harvard.edu

However, there are some issue with this approach...

and high-quality imaging. IA have been explored as a probe of primordial non-Gaussianity (Slepian et al. 2021; Slepian et al. 2023), Baryon Acoustic Oscillations (Okumura et al. 2019; Xu et al. 2022), Redshift Space Distortion (Liu et al. 2017; Liu et al. 2024). In some cases it is advantageous to study the alignment of galaxy multiplets (Liu et al. 2024) as opposed to individuals. The determined shapes of galaxy ensembles are unaffected by the myriad of systematic effects which arise from imaging, and are associated with the shapes of the underlying matter distribution.

I. You need really good pictures of galaxies to precisely measure their shapes (this is hard).

(Smargon et al. 2012; Fornara et al. 2021; Lee et al. 2023). Clusters of luminous red galaxies (LRGs) in the Sloan Digital Sky Survey

(SDSS; Luminous Red Galaxies (LRGs) in the Sloan Digital Sky Survey (SDSS); Smargon et al. 2012; van Uitert & Joachimi 2017). These correlations were found to be lower than predicted by N-body simulations, which may be due to selection bias. The LRGs are more likely to be misidentified as cluster members (Shi et al. 2024). There are

other correlations between clusters, particularly for photometric surveys (Smargon 2022).

2. Many galaxies show no correlation. No one has been able to make this measurement with spiral galaxies.

In this work we explore the potential of using galaxy “multiplets”:

small sets of galaxies, mostly consisting of 2-4 members within 1 $h^{-1}\text{Mpc}$ of each other (Fig. 1). We expect these tiny ensembles to still preserve information from the large-scale tidal field, while being more abundant than larger groups. Multiplets are not necessarily virialized systems, but can be understood in the IA framework as they are well with

...so here's our idea: ...ational evolution. Like galaxy shapes and haloes, their orbital structure carries a memory of the initial tidal field.

The alignment of galaxy multiplets may be a better estimator than the alignment of individual galaxies. This is particularly the case for spiral (or “blue”) galaxies. The latter of these applies to most available spectroscopic samples beyond redshift 1. Understanding the redshift evolution of IA is an important component of fully utilising forthcoming cosmic shear surveys (DES Collaboration and Kilo-Degree Survey Collaboration et al. 2023). However the redshift evolution of IA is unclear and there is no direct IA detection beyond redshift 1 with traditional estimators.

We describe and model this estimator, and compare it to the traditional IA estimator, but this work is also related to the fields of both galaxy groups and higher-order clustering. Although multiplets are not galaxy groups, which are virialized systems and typically describe more complete sets of galaxies (Oppenheimer et al. 2021), multiplets exist on similar scales. The main difference is that multiplets are identified in dense samples. Furthermore, the nonlinear dynamics within groups directly affect the amplitude of multiplet

alignments (Oppenheimer et al. 2021). Multiplets are identified in dense samples. Furthermore, the nonlinear dynamics within groups directly affect the amplitude of multiplet

alignments (Oppenheimer et al. 2021). Multiplets are identified in dense samples. Furthermore, the nonlinear dynamics within groups directly affect the amplitude of multiplet

alignments (Oppenheimer et al. 2021). Multiplets are identified in dense samples. Furthermore, the nonlinear dynamics within groups directly affect the amplitude of multiplet

alignments (Oppenheimer et al. 2021). Multiplets are identified in dense samples. Furthermore, the nonlinear dynamics within groups directly affect the amplitude of multiplet

alignments (Oppenheimer et al. 2021). Multiplets are identified in dense samples. Furthermore, the nonlinear dynamics within groups directly affect the amplitude of multiplet

alignments (Oppenheimer et al. 2021). Multiplets are identified in dense samples. Furthermore, the nonlinear dynamics within groups directly affect the amplitude of multiplet

alignments (Oppenheimer et al. 2021). Multiplets are identified in dense samples. Furthermore, the nonlinear dynamics within groups directly affect the amplitude of multiplet

alignments (Oppenheimer et al. 2021). Multiplets are identified in dense samples. Furthermore, the nonlinear dynamics within groups directly affect the amplitude of multiplet

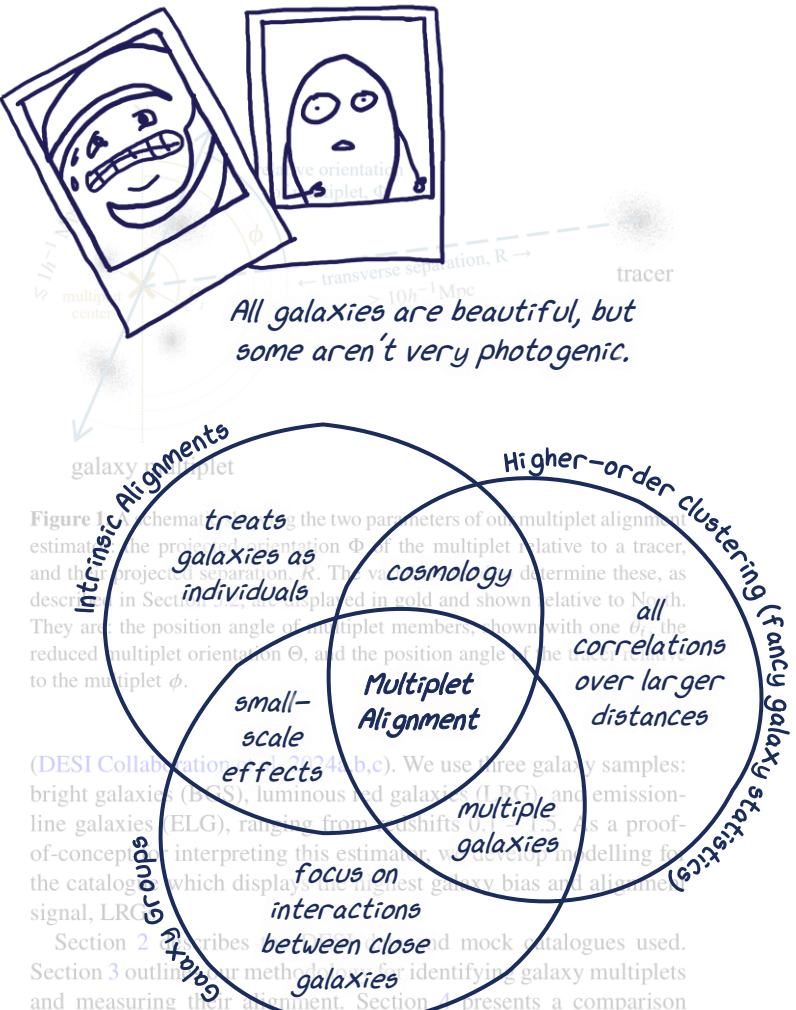


Figure 1: A schematic diagram illustrating the two parameters of multiplet alignment estimation. The diagram shows the projected orientation Φ of the multiplet relative to a tracer, and the various angles used to determine these, as described in Section 3.2, displayed in gold and shown relative to North. They are the position angle of multiplet members, shown with one of the reduced multiplet orientation Θ , and the position angle of the tracer relative to the multiplet ϕ .

DESI Collaboration (2024a,b,c). We use three galaxy samples: bright galaxies (BGS), luminous red galaxies (LRG), and emission-line galaxies (ELG), ranging from redshifts 0.6 to 1.6. As a proof-of-concept for interpreting this estimator, we develop modelling for the catalogues which displays the highest galaxy bias and alignment signal, LRGs.

Section 2 describes the data and mock catalogues used. Section 3 outlines our method for identifying galaxy multiplets and measuring their alignment. Section 4 presents a comparison to mock catalogues and an analytic model of the alignment signal. Section 5 summarizes key results and discusses prospects for utilising future datasets.

This idea is built upon the work of past scientists and has many connections to it.

$$H_0 = 69.6, \Omega_{m,0} = 0.286, \Omega_{\Lambda,0} = 0.714.$$

WHERE DOES OUR DATA COME FROM?

2 DESI CATALOGUES

DESI’s targets are chosen from DR9 of the Legacy Imaging Survey (Dey et al. 2019; Myers et al. 2023). For more information on DESI’s target selection, see DESI Collaboration et al. (2023a,b). We use spectroscopic redshifts from DESI’s Real 1 data (Guy et al. 2023; Schlafly et al. 2023). This data will be publicly available with DESI’s Data Release 1 (DR1) (DESI Collaboration 2025), and doc-

umented in DESI Collaboration (2024). This data will be publicly available with DESI’s Data Release 1 (DR1) (DESI Collaboration 2025), and doc-

umented in DESI Collaboration (2024). This data will be publicly available with DESI’s Data Release 1 (DR1) (DESI Collaboration 2025), and doc-

umented in DESI Collaboration (2024). This data will be publicly available with DESI’s Data Release 1 (DR1) (DESI Collaboration 2025), and doc-

umented in DESI Collaboration (2024). This data will be publicly available with DESI’s Data Release 1 (DR1) (DESI Collaboration 2025), and doc-

umented in DESI Collaboration (2024). This data will be publicly available with DESI’s Data Release 1 (DR1) (DESI Collaboration 2025), and doc-

umented in DESI Collaboration (2024). This data will be publicly available with DESI’s Data Release 1 (DR1) (DESI Collaboration 2025), and doc-



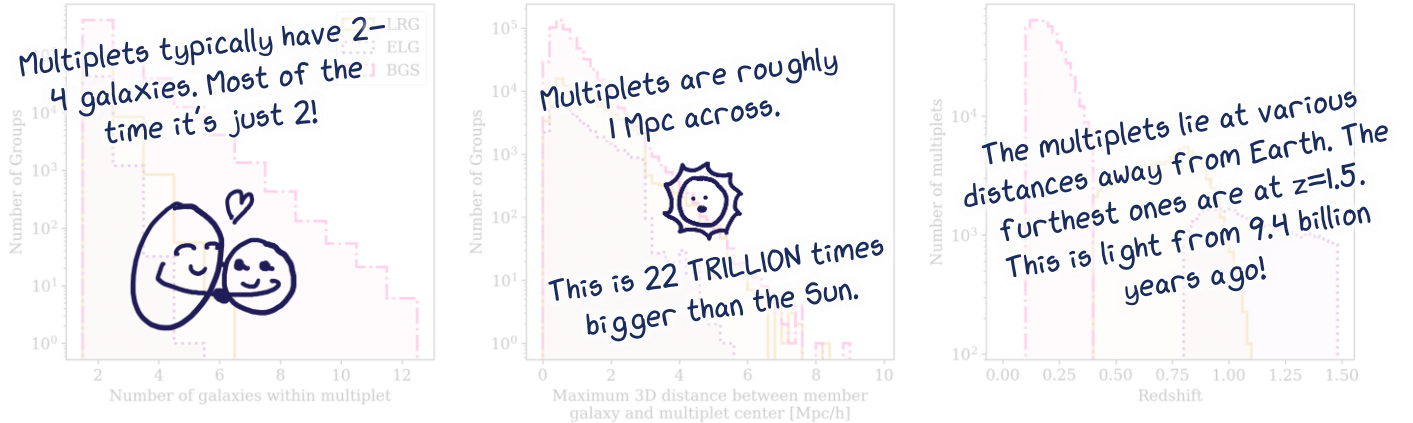


Figure 2. These plots show information about the galaxy multiplets we find, composed of only two members, even for the densest sample, BGS, where 70% of multiplets are galaxy pairs. The spatial size of multiplets is shown in the middle panel, which is described by the maximum 3D distance between member galaxies. The right panel shows the redshift distribution of multiplets.

Galaxy type	Redshift Range	N galaxies	N multiplets	Volume [Gpc $^3 h^{-1}$]
Type of Galaxy				
ELG	$0.1 < z < 1.5$	5 M	21 K	67.8
ELG	$0.8 < z < 1.1$	1.2 M	22 K	35.8
BGS	$0.4 < z < 1.1$	2.2 M	105 K	34.6
How far away they are				
			"close"	
			far away	
			REALLY far away	
How dense the sample is				
ELG	$0.3 < z < 0.4$	0.6 M	64 K	3.2
BGS	$0.1 < z < 0.2$	1.4 M	12 K	0.5
BGS Blue	$0.1 < z < 0.2$	0.56 M	307 K	0.5
BGS Red	$0.1 < z < 0.2$	0.54 M	100 K	0.5

Table 1. Properties of the DESI catalogues used to identify galaxy multiplets. The right column shows the comoving volume of the sample, estimated from the positions of galaxies in the data. The color selection used to make the BGS Blue and Red samples are described in Section 2.

We found multiplets using samples of many types of galaxies!

3 ALIGNMENT METHOD

3.1 Identifying galaxy multiplets

Our measurement is a projected quantity, along the orientation of multiplets in the plane of the sky as a function of transverse distance (Figure 1). However, we identify small multiplets of galaxies in 3D comoving space using spectroscopic redshifts. Each galaxy is matched to its nearest neighbour and all pairs are limited to a maximum separation in the plane of the sky, r_p , and along the line of sight, r_{\parallel} . r_{\parallel} is necessarily larger than r_p to account for the redshift-space distortions created by peculiar velocities of multiplet members. We then find multiplets within these matches using the Friends-of-Friends algorithm to identify sets of galaxies (Geller & Fisher 1964). We set no maximum for the number of multiplet members. This is similar to the friends-of-friends algorithm used for identifying haloes in N-body simulations and for constructing group catalogues (Davis et al. 1985; Eke et al. 2004; Robotham et al. 2011). Note that unlike these catalogues, our goal is not to identify complete, gravitationally bound objects. We expect even nonvirialized objects to contribute to our final measurement and so set no additional criteria such as completeness or velocity dispersion.

To explore the effectiveness of this algorithm to identify distinct multiplets, we created a catalogue of isolated multiplets, consisting only of multiplets where each member was a minimum of $2r_p$ and $2r_{\parallel}$ away from the nearest non-multiplet member. This had no significant effect on final results. We tested multiplets constructed from varying criteria, between $0.5 < r_p < 12 h^{-1} \text{Mpc}$ and $0.5 < r_{\parallel} < 12 h^{-1} \text{Mpc}$. We found no significant effect on the amplitude of the final signal when varying these parameters, so we selected cuts to maximize the signal-to-noise ratio. We model in Section 4, LRGs. For all samples, we use $r_p = 1.0 h^{-1} \text{Mpc}$ and $r_{\parallel} = 6.0 h^{-1} \text{Mpc}$. At this point, such as scale cuts which depend on density or removing very close pairs (see Section 4.1) may improve the SNR and are worth exploring in future works.

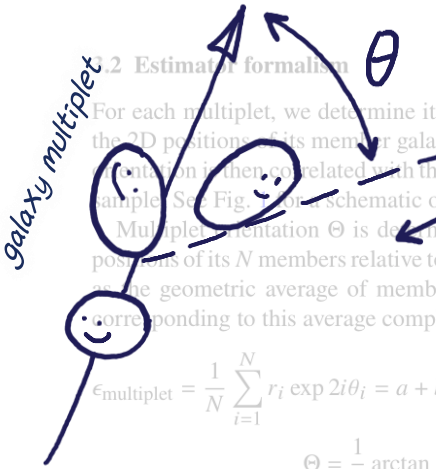
This page shows information

Properties of the DESI samples we identified multiplets in are shown in Table 1. The histograms shown in Fig. 2. This displays the number of members within each multiplet, which is most often two. It also shows the spatial size of each mul-

WHAT ARE MULTIPLETS AND HOW DO WE FIND THEM?
Multiples are little sets of galaxies: as in a doublet, triplet, quadruplet, etc.
We find them by using the 3D positions of galaxies measured by DESI. The basic idea is to find the closest neighbor to each galaxy and then use an algorithm to identify sets within those connections.

WHAT EXACTLY ARE WE MEASURING?

... by taking the maximum 3D distance between a multiplet member and the multiplet's centre in redshift space. Note that this can be greater than r_p and r_{\parallel} since we only limit the distance between multiplet members, not its overall size.



For each multiplet, we determine its projected orientation based on the 2D positions of its member galaxies in the plane of the sky. This orientation is then correlated with the position of galaxies in a tracer sample. See Fig. 1 for a schematic of the variables used.

Multiplet orientation Θ is determined by averaging the complex positions of its N members relative to its centre. This centre is defined as the geometric average of member 2D positions. Θ is the angle corresponding to this average complex number:

$$\epsilon_{\text{multiplet}} = \frac{1}{N} \sum_{i=1}^N r_i \exp 2i\theta_i = a + bi$$

$$\Theta = \frac{1}{2} \arctan \frac{b}{a}$$

For each member i , r_i is the projected distance to the multiplet centre

Our measurement comes down to two numbers: We do not consider the full ellipticity of the multiplet, i.e. axis ratio, because it is meaningless for multiplets with two members and it is not expected to increase our signal-to-noise ratio. For single galaxies, measurements with the SDSS-III BOSS LOWZ sample have found that ... (see Fig. 10 in this paper).

I. The orientation of a multiplet relative to a tracer, Θ This orientation angle is then measured relative to the tracer sample. In most cases, the tracer sample is the same as the one used to identify multiplets. For each pair, consisting of a galaxy multiplet and a tracer, the angle between the position

2. The distance between a multiplet and a tracer, R The angle between the position angle of the multiplet relative to the tracer, ϕ , and the multiplet's orientation:

We find millions of multiplet-tracer pairs and find the average orientation as a function of separation.

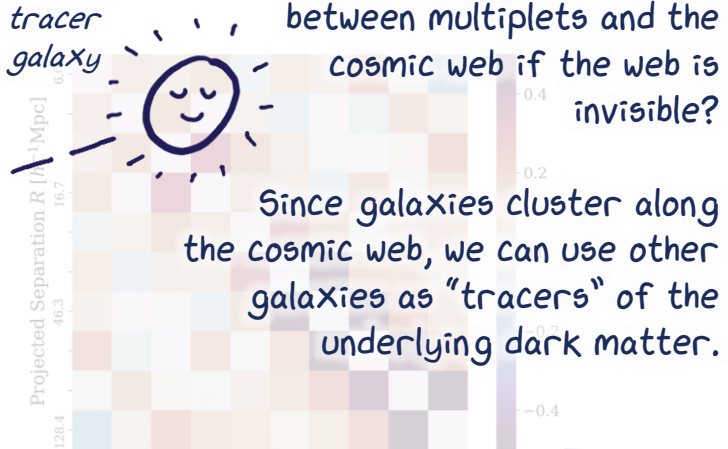
We expect that multiplets will "point" towards areas of high density, as traced by other galaxies. And that the effect will be strongest when a multiplets is close to a tracer.

3.3 close to a tracer. Just like long galaxies!

When measuring the projected orientation of multiplets relative to a tracer catalogue, we limit the multiplet-tracer pairs to a line-of-sight separation that is unique to each bin of projected separation, $\Pi_{\max}(R_{\text{bin}})$. This is to maximise the signal-to-noise of our measurement. In the case of positive tidal alignment, shapes are elongated along the stretching direction of the tidal field. In this situation, the tidal field along the line of sight has a measurable orientation in the plane of the sky. Therefore, multiplet-tracer pairs that are close in the plane of the sky but distant along the line-of-sight direction will have a relatively low contribution to the total alignment.

WHAT ARE THE MEASUREMENTS? The measurement are.... On the next page! But there's a sneak-peak here.

How do we measure correlations between multiplets and the cosmic web if the web is invisible?



Since galaxies cluster along the cosmic web, we can use other galaxies as "tracers" of the underlying dark matter.

If a multiplet points towards a tracer $\rightarrow \Theta = 0 \rightarrow \cos(2\Theta) = 1$

(1) If multiplets have random orientations, on average: $\rightarrow \cos(2\Theta) = 0$

Figure 3. The reduced covariance matrix corresponding to the LRG signal

(1) If multiplets have random orientations, on average: $\rightarrow \cos(2\Theta) = 0$

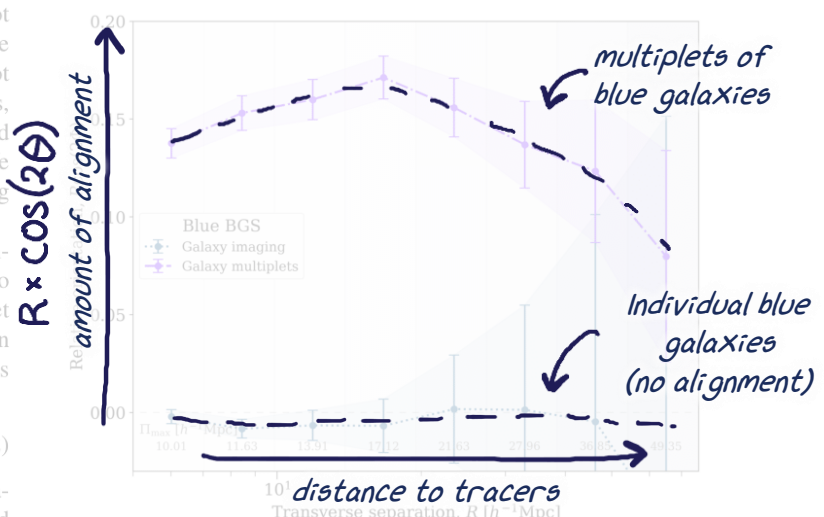
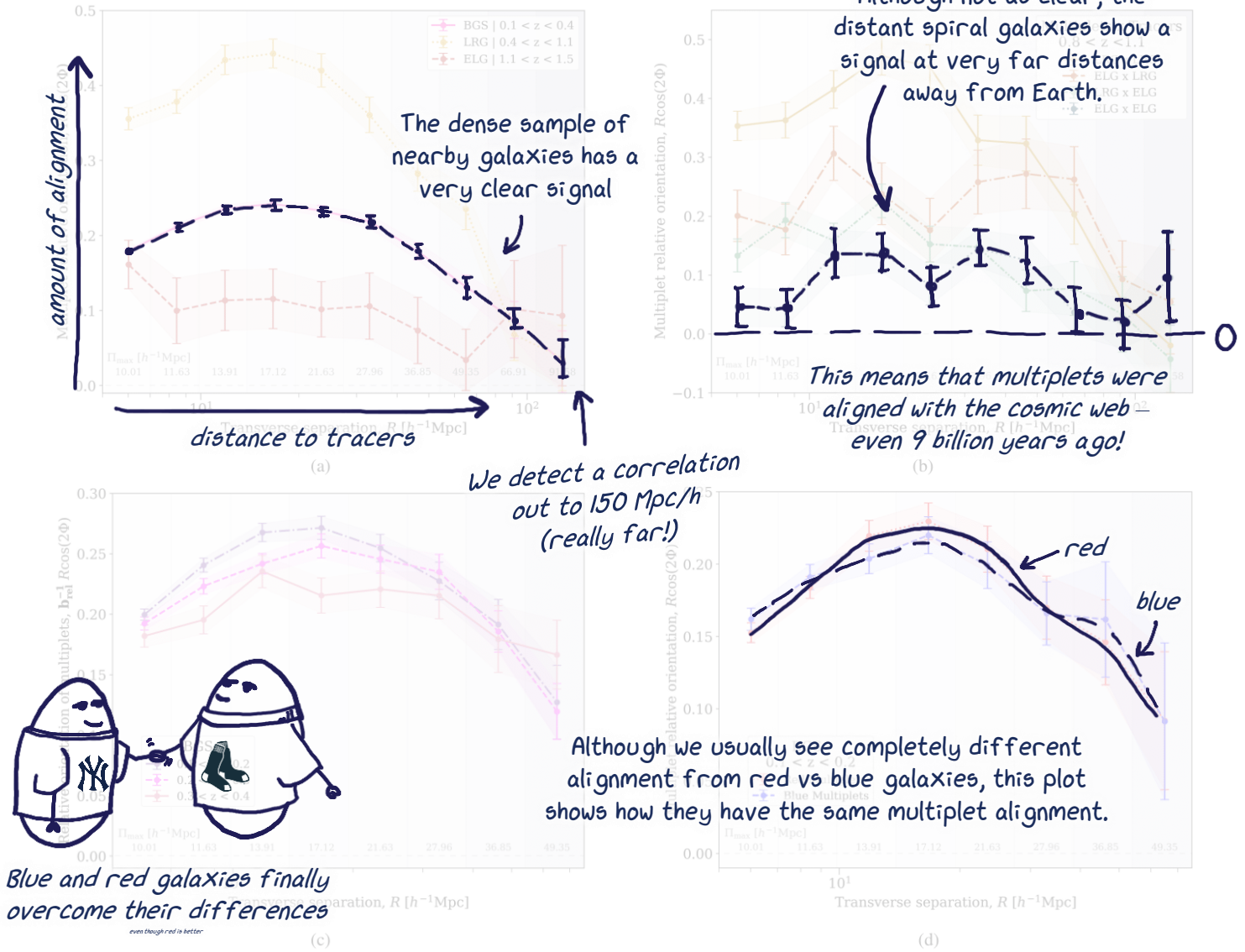


Figure 4. A demonstration of the advantages of using multiplet alignment. Here we show the tidal alignment of galaxy and multiplet orientations within a dense, blue sample. The alignment of galaxies is highly sensitive to their orientation and the expected correlation with the cosmic web. Here we show how we can detect a correlation to the cosmic web using multiplets of blue galaxies.

This is much better than the alignment of individual blue galaxies, which is 0. The signal is due to the tidal field, which is proportional to the distribution of galaxies and the projected separation. We chose $\Pi_{\max}(R_{\text{bin}}) = 6h^{-1}\text{Mpc} + \frac{2}{3}R_{\text{bin}}$ based on the signal-to-noise ratio of our final LRG signal. Our model estimate is computed in these same R bins. Throughout plots in this paper, the varying values of Π_{\max} are shown through shaded regions and marked explicitly. We use this projected statistic, as opposed to keeping the measurement as a function of r_p and r_{\parallel} , because most of the signal is along the LOS for tidal alignments due to the projection of shapes. Additionally, a projected statistic allows for more direct modelling as it is less sensitive to redshift-space distortions (Figure 7).

For each measurement, we separate the multiplet catalogue into 100 sky regions by right ascension and declination, with equal numbers of multiplets in each. The orientation of multiplets is measured



Our measurements reveal that multiplets are indeed aligned with the cosmic web!!

These plots are the result of us playing around and making this measurement with many types of galaxies. Here I've highlighted a few interesting results.

Figure 5. Correlations between the projected orientations of galaxy multiplets and density for different galaxy samples as a function of projected separation, R . The measurement in each bin utilises a different value of Π_{max} , indicated by the shaded regions and marked at the bottom of each plot. Π_{max} is the maximum line-of-sight distance between a multiplet-tracer pair. Unless otherwise stated, each measurement uses the same catalogues of multiplet orientations and density tracers. (a) The signal is clearest for the BGS sample, and their signal is the one we focus on reproducing in Section 4. The signal is especially clear for the dense BGS sample. Although a sparse sample, we also detect a signal with ELGs beyond redshift 1. (b) displays the alignment of multiplets in red and blue subsamples of the lowest redshift BGS galaxies relative to the full BGS sample. We find no obvious difference in scale dependence, demonstrating the potential of utilising blue

separately in each region, but relative to the full tracer sample. Our final measurement is the mean and standard error of these 100 measurements for the densest redshift subset (BGS), we use 147 regions. To account for this, for each measurement, we also compute the average signal in each R_{bin} before averaging over the multiple random catalogues. This marginally increases the measurement noise but is more practical for samples with many multiplet-tracer matches.

This shows that tiny groups of galaxies still have some memory of the large-scale structure connected to their formation in the early universe.

We find the signal to be sensitive to survey geometry on large scales. To account for this, for each measurement, we also compute the orientation of galaxy multiplets relative to random catalogues designed to match DESI's Y1 footprint. The range of multiplet separations we consider is roughly 10^1 to $10^2 h^{-1}$ Mpc. We use multiple random catalogues to account for the footprint of the survey. Across samples, we see a turnover in the multiplet-random signal around $80 h^{-1}$ Mpc. We see no evidence of anisotropy in the orientations of multiplets, so this systematic "tangential alignment" at large separations is likely to be due to the footprint of the tracers, which spans a narrow band in right ascension. This pattern is not present when measuring the signal in isolated square regions.

Now onto the hard part, interpreting the measurements...

WHAT DOES ALL THIS MEAN?

The rest of our paper explores what is actually happening in the universe to create these correlations. Our goal is to quantitatively connect our measurements to the cosmic web. At dependence. For each measurement, we use the same galaxies to construct multiplets and the tracer catalogue. The exception is the overlapping LRG and ELG region of $0.8 < z < 1.1$, where we measure each cross-correlation between the samples (Fig. 5b). Although we expect each of these signals to display a similar scale dependence, we find that the alignment signal for the BGS sample is significantly lower than the alignment signal for the highest-redshift ELG bin at $1.1 < z < 1.5$. This is likely due to the lack of alignment signal in the LRG sample, which we have made no adjustment for clustering differences between samples; this plot demonstrates the alignment strength and scale dependence of the multiplet alignment measurements can be found in Fig. 5, and the covariance matrix for the LRG multiplet alignment in Fig. 3. Within the four bins we used to scale our model in Section 4, between 20 - 100 h $^{-1}$ Mpc, the alignment signal decreases by about 1.8 σ .

A challenging part of this is that stuff on small scales behaves differently than stuff on large scales.

We split the sample into two sets of samples (Fig. 5c). In this plot we account for the galaxy bias and its evolution across redshifts. Intrinsic properties of BGS also vary across redshift, so this plot should not be interpreted as a redshift evolution. For instance, the highest redshift bins contains the most luminous galaxies, which are known to display higher alignment. Despite this, the highest signal comes from low-mass, low-redshift galaxies. Galaxies in the lowest redshift bin have stellar masses of around $10^{10} M_{\odot}$ (Hahn et al. 2020). Fig. 5 shows the multiplet alignment signal vs redshift in this same sample. The colour cuts selection of these subsamples are described in Section 2 and their alignments were measured relative to the full BGS catalogue. The blue and red samples display similar redshifts and scale dependences. This shows that blue galaxies can be used to trace the tidal field of red galaxies, which is a promising result for measuring alignment beyond redshift 1.

To cosmologists, galaxies are just 'lil guys' individual galaxies are well-suited to samples that are especially dense and samples of blue galaxies. To directly demonstrate this, within the BGS Blue sample we measure the intrinsic alignment of individual galaxies using imaging from the Legacy Imaging Survey. Here we find some evidence for alignment geometry. This is accounted for through the large statistical error at large separations. As expected, the alignment of these faint blue galaxies is consistent with zero at all separations. However, galaxy multiplets in the same catalogue display a clear alignment signal (Fig. 4).

COMPARING TO SIMULATIONS

4 INTERPRETATION

In this Section we explore the modelling of multiplet alignments through simulations and theory, using the LRG sample as a case study. This is because LRGs have a large galaxy bias, they display different orientations, and there exist associated DESI mocks that are designed for reproducing the alignment of large-scale structures.

4.1 Comparison to simulations

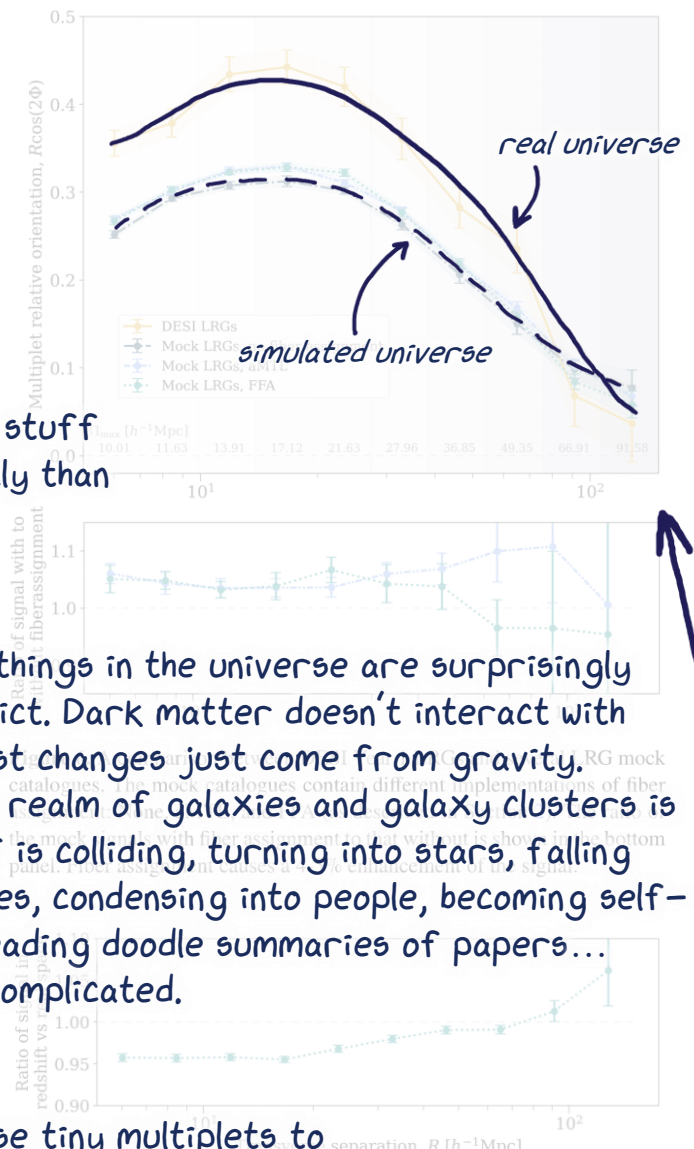
The simulations we use are designed to reproduce statistics about the universe on very large scales. So they only include dark matter.



The biggest things in the universe are surprisingly easy to predict. Dark matter doesn't interact with itself, so most changes just come from gravity. However, the realm of galaxies and galaxy clusters is messy. Stuff is colliding, turning into stars, falling into black holes, condensing into people, becoming self-aware and reading doodle summaries of papers... It's all very complicated.

So how do we connect these tiny multiplets to the largest structures in the universe?

Figure 7. This is an assessment of the impact of RSD on the multiplet alignment signal. Here we plot the ratio between the aMTL signal in Fig. 6 and a version where the shape-tracer correlations were measured in real space. The two measurements differ by about 5% on these scales.



average measurement of 25 simulations for each mock catalogue and their standard deviations. The LRG signal is 'blown up' in Fig. 6. We find no significant difference in the number of multiplets found, but it is slightly higher for the aMTL signal. This probably reflects the fact that the simulation catalogues include non-Gaussian clustering effects. However, they sufficiently reproduce the shape of the signal.

aMTL is the most realistic simulation of fiber assignment, but we do not find a significant difference between the two mock catalogues which include fiber assignment. It is interesting to note that the signal is marginally higher for the fiber assignment catalogues, which can be seen in the lower panel of Fig. 6. This is probably because galaxies very close to a multiplet's centre are more affected by nonlinearity dynamics and therefore have stronger correlations. Individual galaxies display higher alignment in their outer regions for the same reason (Singh & Mandelbaum 2016; Georgiou et al. 2019).



I don't know what you're talking about, Dave.

You shouldn't always trust computers....

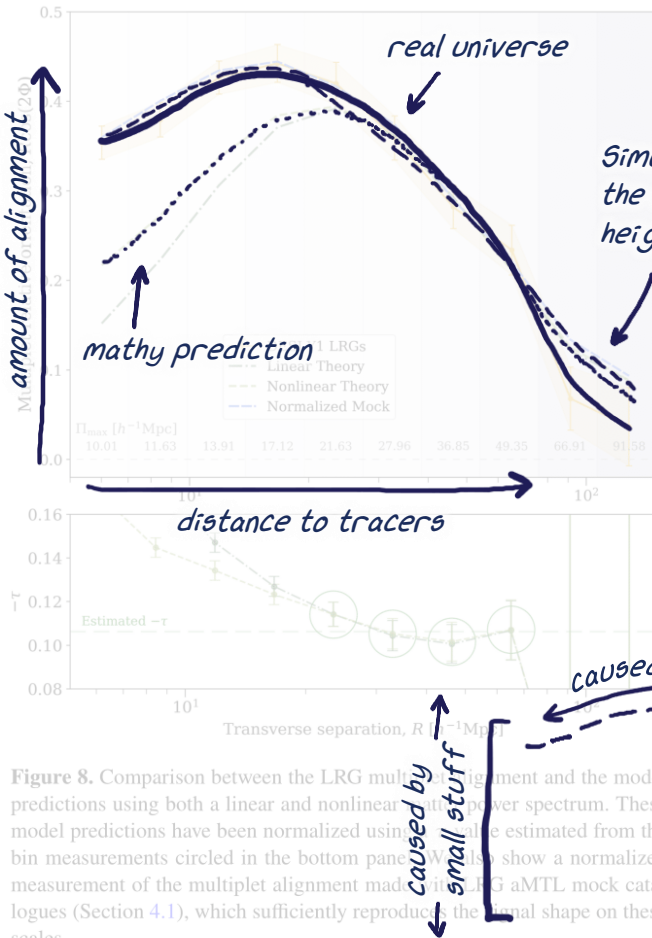


Figure 8. Comparison between the LRG multiplet alignment and the model predictions using both a linear and nonlinear matter power spectrum. These model predictions have been normalized using the value estimated from the bin measurements circled in the bottom panel. We also show a normalized measurement of the multiplet alignment made with LRG aMTL mock catalogues (Section 4.1), which sufficiently reproduce the signal shape on these scales.

The shape of our measurement is a result of the big stuff – cosmic web. The amplitude is a result of the small stuff – how galaxies move around each other.

removing some of this dilution, we find that this separation of the initial pairs needed to make the LRG multiplet set analogue to $r_p > 0.5 h^{-1} \text{Mpc}$ and find a similar enhancement of the signal, 10% between $6 - 60 h^{-1} \text{Mpc}$. This may be a useful addition to future studies of multiplet alignment.

We do not include the effects of RSD in our analytic model (Section 4), so to test this assumption we reproduce the aMTL measurement in real space. Here, galaxy multiples are still found in redshift space, but the multiplet-tracer correlations are measured using the true positions of the multiplet centres and tracers. The effects of RSD on the tracer catalogue appear to make a 0 – 5% difference on scales beyond $10 h^{-1} \text{Mpc}$ (Fig. 7).

INTERPRETATION WITH MATH

4.2 Modeling

To quantify the connection between multiplet orientation and the underlying matter distribution, we assume a linear relationship between shapes.

Besides simulations, we can also use math!
Here we model the 3D gravitational field created by large-scale structure and then derive an equation which describes how different components in the universe combine to produce our measurement.

Following the convention in Liddle et al. (2020, 2024), we

describe the traceless tidal tensor as

$$T_{ij} = \partial_i \partial_j \phi - \frac{1}{3} \delta_{ij}^K \nabla^2 \phi, \quad (3)$$

where $\nabla^2 \phi \propto \delta$ is given by the Poisson equation, with δ being the amplitude of the correlation function. The signals are not the same height, but have the same shape!

$$T_{ij}(\vec{r}) = \int \frac{d^3 k}{(2\pi)^3} \left(\frac{k_i k_j - \frac{1}{3} \delta_{ij}^K k^2}{k^2} \right) \tilde{\delta}_m(\vec{k}) e^{i\vec{k} \cdot \vec{r}}, \quad (4)$$

where we have used $\tilde{\delta}$ to indicate a variable in Fourier space. Our measured signal is a projected quantity, where we define \hat{z} to be along the line-of-sight. Therefore, for a projection with $\alpha, \beta = \{x, y\}$ and using the relation $T_{xx} + T_{yy} = -T_{zz}$, the relevant projection of the tidal field is $(T_{\alpha\beta} + T_{zz}/2)$.

In this study we characterize the relevant “shapes” of objects solely by orientation, instead of the full ellipticity. This axis-ratio component of shapes affects the amplitude of the signal as does any systematic misalignment of galaxy multiplets to the large-scale field caused by local dynamics. Our focus in this work is to explore how multiplet alignment traces the tidal field across large scales, without making any assumptions about the effect’s amplitude. Therefore, we fold in the full ellipticity information and any misalignment effects into the signal amplitude, assuming neither display scale dependence at large separations. This is similar to the “stick model” employed for describing the positions and alignments of galaxies within haloes (Fortuna et al. 2021; Schneider & Bridle 2010).

The projected ellipticity of galaxy multiplets can be described by the traceless tensor

$$\epsilon_{\alpha\beta} = \tau (T_{\alpha\beta} + \frac{1}{2} T_{zz}). \quad (5)$$

in Section 3.2, and τ is a parameterization of the shape’s response to the tidal field. It includes any effects from the full-shape information and any misalignment effects due to the tidal direction. The full complex ellipticity is described as

$$\epsilon = \tau [T_{xx} - T_{yy} + 2iT_{xy}]. \quad (6)$$

The quantity of interest is the expectation value of the cross-correlation between projected shapes and the matter field, Q :

$$\mathcal{E}_{\text{model}} = \frac{1}{2} \langle \epsilon^* Q + \epsilon Q^* \rangle. \quad (7)$$

We describe the 3D matter field in a particular bin of transverse separation R_{bin} and line-of-sight separation $\pm \Pi_{\text{max}}$ as

$$Q(R_{\text{bin}}, \pm \Pi_{\text{max}}) = \frac{\int d^3 r W(\vec{r}) \delta_g e^{2i\theta_r}}{\int d^3 r W(\vec{r}) (1 + \xi_{\epsilon g})}. \quad (8)$$

Here, δ_g is the fractional matter overdensity, $\xi_{\epsilon g}$ is the shape orientation – galaxy correlation function, r is the 3D separation, and θ_r is the 3D relative angle. $W(\vec{r})$ is a function representing the bin

function, both an annulus in R and $\pm \Pi_{\text{max}}$. \vec{r} is used to denote a binned quantity. The expansion of ϵ in terms of Q can be found in Appendix A, and results

$$\mathcal{E}_{\text{model}} = \frac{-\tau}{\int d^3 r W(\vec{r}) (1 + \xi_{\epsilon g})} \int d^3 r W(\vec{r})$$

$$\int \frac{dk_z}{2\pi} \int K_d K_J_2(KR) \frac{K^2}{k^2} P_{gm}(k) e^{ik_z z},$$

where J_2 is the second Bessel function of the first kind and $P_{gm}(k)$

is the galaxy-matter power spectrum. k represented 3D position in Fourier space, K represents the 2D position on the plane of the sky (k_x, k_y), and k_z lies along the line of sight. $k^2 = K^2 + k_z^2$.

The remainder of this Section describes how we compute Equation 9, by breaking it into the components we measure or calculate. Beginning with the denominator,

$$\int d^3r W(\bar{r})(1 + \xi_{\epsilon g}) = \pi(R_{\max}^2 - R_{\min}^2)(2\Pi_{\max} + \bar{w}_P).$$

\bar{w}_P is the integrated 2-point cross-correlation function between the multiplet and tracer catalogue, $w_P(R)$, within an annulus of R_{\min} and R_{\max} :

$$\bar{w}_P(R_{\text{bin}}) = \frac{1}{\pi(R_{\max}^2 - R_{\min}^2)} \int_{R_{\min}}^{R_{\max}} 2\pi R dR w_P(R). \quad (11)$$

We further define \mathcal{J}_2 , a binned version of the second Bessel function integrated over a given R_{bin} :

$$\mathcal{J}_2(K) = \frac{2}{(R_{\max}^2 - R_{\min}^2)} \int_{R_{\min}}^{R_{\max}} R dR J_2(KR), \quad (12)$$

This can be solved analytically (Equation A8). Using the relation

$$\frac{1}{2\Pi_{\max}} \int_{-\Pi_{\max}}^{\Pi_{\max}} dz e^{ik_z z} = \text{sinc}(k_z \Pi_{\max}), \quad (13)$$

we further define an expression of the relevant matter distribution for a given Π_{\max} :

$$\mathcal{P}_{\Pi}(K) = 2\Pi_{\max} \int \frac{dk_z}{2\pi} \frac{K^2}{K^2 + k_z^2} (\text{the signal we measure}) \quad (14)$$

In practice, for this we use the matter power spectrum and galaxy bias $b_g P_{mm}(k)$, with $b_g = 1.99$ for DESI LRGs (Mena-Fernandez et al. 2024). Combining these expressions, the model prediction for our signal $\mathcal{E}(R)$ is simplified to

$$\mathcal{E}_{\text{model}}(R) = \frac{-\tau}{(2\Pi_{\max} + \bar{w}_P)} \int K dK \mathcal{J}_2(K, R) \mathcal{P}_{\Pi}(K). \quad (15)$$

We compute this numerically in bins of (R_{\min}, R_{\max}) with the corresponding Π_{\max} value in each. The model prediction made with both a linear and nonlinear matter power spectrum can be seen in Fig. 8. The power spectra are from ABACUSUMMIT and evaluated at $z = 0.8$. We normalize the models by taking their ratio to the large-scale signal, using the points circled in the lower panel of Figure 8. This results in an estimate τ for the LRG multiplets of -0.106 ± 0.002 for both LA and NLA. We find that these models can sufficiently match the shape of our measurement only down to scales of $20 h^{-1}\text{Mpc}$, while the LRG mock catalogue matches below $10 h^{-1}\text{Mpc}$. The corresponding τ value for this mock is also -0.106 ± 0.002 . Therefore the NLA model is sufficient for very large scales, but fails to capture the non-linear dynamics between multiplets and tracers in the way that an N-body simulation can.

The alignment amplitude is often characterized with A_{IA} (Catelan & Porciani 2001; Hirata & Seljak 2004; Blazek et al. 2015). A_{IA} describes the relationship between intrinsic galaxy shear, γ_{ij}^I , with the tidal tensor, T_{ij} , as defined in Eq. 3. In the case of “early alignment”, it is assumed that shapes are aligned at time of formation and then evolve with the matter field.

$$\gamma_{ij}^I = -A_{IA}(z) C_1 \frac{\rho_{m,0}}{D(z)} T_{ij} \quad (16)$$

Here, $\rho_{m,0}$ is the matter density, $D(z)$ is the growth factor, normalized so $\bar{D}(z) = (1+z)D(z)$ is unity at matter domination, and C_1 is a

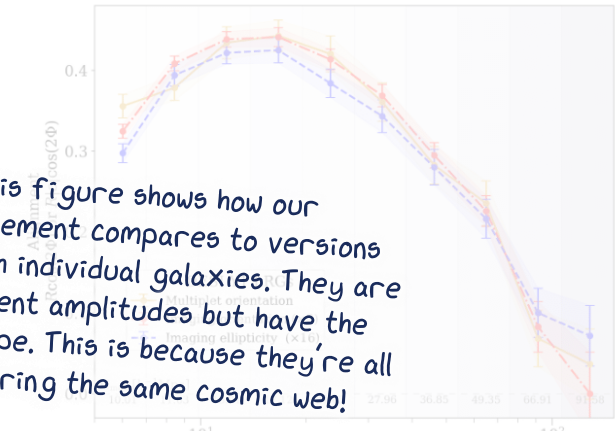


Figure 9. Here we compare the alignment of galaxy multiplets to the alignment of individual galaxies. The yellow line shows the alignment of the orientations of PG multiplets relative to positions of random sample (Section 3.2). The red line is the orientations of individual LRGs relative to an easier comparison. These two measurements model shapes as “sticks”, described only by orientation. The blue line is the full shape alignment of LRGs, taking into account galaxy axis ratio and multiplied by 16 comparison. The bottom panel shows the difference in the points plotted above, highlighting the similar scale-dependence of each estimator. The average signal-to-noise for each of these measurements alone is 9.0 for imaging, and 11.0 for imaging with ellipticity. These measurements were made with 105 thousand multiplets and 2.2 million individual LRGs.

$$\mathcal{E} = \frac{-\tau}{(2\Pi_{\max} + \bar{w}_P)} \int K dK \mathcal{J}_2(KR) \mathcal{P}_{\Pi}(K) \quad (17)$$

historical normalization constant $A_{IA}(z) = -\frac{\tau}{C_1} \frac{D(z)}{\rho_{m,0}}$ (Brown et al. 2015). The relationship to our alignment amplitude τ is

For our “stick” model of LRG multiplets, this corresponds to an average value of $A_{IA} = 5.7 \pm 0.1$. For reference, the corresponding stick alignment of the same sample using individual galaxies and Legacy Survey Imaging is $A_{IA} = 1.96 \pm 0.001$, about 5 times higher than when using the full-shape information (Fig. 9). For this measurement we use the ellipticity definition

$$\epsilon_+ = \frac{a - b}{a + b} \cos 2\theta, \quad (18)$$

based on the galaxy major and minor axis, a and b , and orientation, θ .

Fig. 9 is also a useful demonstration of how, although very different amplitudes, the alignment of multiplet orientation has the same scale dependence of shape alignment and can be modeled similarly. Additionally, multiplet alignment produces a comparable signal-to-noise measurement as full shape alignment, with less than 5% of the objects. While multiplet alignment does not necessarily outperform individual galaxies within the LRG sample, it is promising for dense regions or samples that show weaker intrinsic galaxy alignment.

CONCLUSIONS

5 CONCLUSION

In this work we explore the potential of multiplet alignment for large spectroscopic surveys through DESI's real data. These multiplets mostly consist of 2-4 members within 1-10 h⁻¹Mpc of each other. By measuring their orientations relative to the underlying traced tidal field, we detect an intrinsic alignment signal on comoving scales separated by 100 h⁻¹Mpc and beyond redshift 1. The shapes of this galaxy multiplet alignment over the alignment of individual galaxies depend on properties of the galaxy catalogue, including morphology, density, and imaging quality. We find similar signals regardless of galaxy colour or luminosity, which is a promising result for measuring the tidal field with galaxy populations that typically display little or no intrinsic shape alignment.

We come up with a way to describe these correlations and make measurements using samples of different types of galaxies.

Using the LRG sample as a case study, we reproduce the LRG bias in relative shape alignment previously found by Lavaux et al., but match its shape. Using a nonlinear tidal alignment model, we find an amplitude parameter $\tau = -0.106 \pm 0.002$, which characterizes the response of multiplet orientations to the tidal field. This modelling matches the measured signal above scales of 20h⁻¹Mpc but fails to capture nonlinear effects at smaller scales, unlike the N-body prediction.

The multiplet alignment signal could be improved by supplementing multiplet catalogues with imaging, by identifying additional galaxies close to spectroscopic targets. Additional improvements could be made by weighting the shapes of multiplets based on member luminosity, or weighting alignment by multiplet richness. Although we focus on modelling LRGs for this estimator, they are not necessarily the most optimal application. The signal is especially clear for the dense BGS region and warrants further exploration into sub-trends within the population, such as redshift and luminosity dependence.

Compared to measurements of galaxy shape alignments, the use of spectroscopical **distance to tracers** mitigates systematic effects from imaging and shape measurements, and can extend intrinsic alignment studies to samples that do not display intrinsic shape alignments (Fig. 4). The remaining 4 years of the DESI survey will significantly increase the size and comoving density of the ELG sample, allowing for better measurements of intrinsic alignment at higher redshifts.

Although we describe multiplets as distinct objects throughout this work and model their orientations with intrinsic alignment, for dark matter halo shapes, the multiplet alignment estimator is especially a speed-up compared to the full simulation of the evolution of multiplets. In addition, distance to tracers is a very useful tracer of the orientation of the galaxy pair is determined by all nearby galaxies in the same multiplet. This indicates that there is a remnant of nonlinear collapse preserved even into the non-linear regime, at the scales of the multiplet sizes of around 1 h⁻¹Mpc.

In principle, this measurement can be used to produce an intrinsic shear map and reconstruct the underlying matter field. Unlike the shear measurements from weak-lensing, intrinsic shear preserves line-of-sight information. However, the measurements will be affected by the foreground map of the multiplet shapes, polarization, and therefore any inference of the tidal field. An advantage of using galaxy multiples to estimate systematics that are distinct from the galaxy field, and may provide an avenue to more precisely measure large-scale modes.

The difficulty lies in determining the modelling amplitude, $\tau(z)$. This could potentially be determined through hydrodynamic simulations and/or illustrating it via a weak lensing map and an assumed amplitude in the redshift-dependent matter power spectra. Such a mass model may provide a way to constrain the underlying cosmological dependence. With the right sample and understanding of the modelling amplitude, this could be a unique way to explore the large-scale matter field in future surveys.

ACKNOWLEDGMENTS

The authors wish to acknowledge useful conversations with Jonathan Blazek, Frédéric Bourguignon, Thomas Park, and Christos Georgiou at the LILAC workshop, held at the Center for Astrophysics | Harvard & Smithsonian. They also thank the DESI internal reviewers, Carolina Cuesta, Azaro and Jiamin Hou for feedback on the paper.

This material is based upon work supported by the U.S. Department of Energy under grant DE-SC0013718, NASA under ROSES grant 12-EUCLID12-0004, and the Simons Foundation.

This material is based upon work supported by the U.S. Department of Energy (DOE), Office of Science, Office of High-Energy

The shape of the resulting measurement is a result of the underlying cosmic web, and is the same regardless of what types of galaxies we use. We can predict this shape using simulations of dark matter.

The height of the measurement is a result of smaller effects: how galaxies move around each other in the little groups. This part is harder to model.

<https://www.desi.lbl.gov/collaborating-institutions>

DESI Legacy Imaging Survey (DELS) consists of individual

surveys: the Dark Energy Camera Legacy Survey (DECaLS), the

Beijing-Arizona Sky Survey (BASS), and the Mayall z-band Legacy Survey (MzLS). DECaLS, BASS and MzLS together include data obtained, respectively, at the Blanco telescope,

Cerro Tololo Inter-American Observatory, NSF's NOIRLab; the Bok

telescope, Steward Observatory, University of Arizona; and the M

an telescope, Kitt Peak National Observatory, NOIRLab. NOIRLab

is operated by the Association of Universities for Research in As-

tronomy (AURA) under a cooperative agreement with the National

Aeronautics and Space Administration. Pipeline processing and analysis of the data

is performed by NOIRLab and the Lawrence Berkeley National

Laboratory. Legacy Surveys also uses data products from the Near-

Earth Asteroid Rendezvous Infrared Survey Experiment (NEOWISE),

a joint project of the Jet Propulsion Laboratory/California Institute of Technology, funded by the National Aeronautics and Space Admini-

stration. Legacy Surveys was supported by: the Director, Office of

Science, Office of High Energy Physics of the U.S. Department of

Energy; the National Energy Research Scientific Computing Center,

a DOE Office of Science User Facility; the U.S. National Science

Foundation, Division of Astronomical Sciences; the National Astro-

nomic Observatory; the National Science Foundation, Office of Sciences

and the Chinese National Natural Science Foundation. BNL is man-

aged by the Regents of the University of California under contract to

the U.S. Department of Energy. Complete acknowledgments can

be found at <https://www.legacysurvey.org/>.

Any opinions, findings, and conclusions or recommendations ex-

But wait, there's (always) more!

**Our acknowledgement section is as long as the conclusions!
It takes the support of many organizations and people to
make a big survey like DESI possible.**

pressed in this material are those of the author(s) and do not necessarily reflect the views of the U.S. Department of Energy or any of the listed funding agencies. The authors are honored to be permitted to conduct scientific research on Iolkam Du'ag (Kitt Peak), a mountain with particular significance to the Tohono O'odham Nation.

SEE THE DATA YOURSELF

DATA AVAILABILITY

The DESI Legacy Imaging Survey is publicly available at legacysurvey.org. You can find the publicly available data we used here at data.desi.lbl.gov/doc/releses/dr1/. It covers the DESI Year 1 sample and will be released as part of DESI Data Release 1 (DESI Collaboration 2025). ABACUSSUMMIT simulations are available at abacusbody.org.

Data plotted in this paper can be downloaded from zenodo.org/records/13230864.

PAPERS WE REFERENCE

REFERENCES

- A. Ross et al. 2024, in preparation
- Akitsu K., Kurita T., Nishimichi T., Takada M., Tanaka S., 2021, *Physical Review D*, 103, 063531
- Akitsu K., Li Y., Ohmura T., 2023, *Physical Review D*, 107, 063531
- Blazek J., 2014, *Journal of Cosmology and Astroparticle Physics*, 2014, 015
- Bridle S., King L., 2007, *New Journal of Physics*, 9, 444
- Brown M. L., Taylor A. N., Hambly N. C., Dye S., 2002, *Monthly Notices of the Royal Astronomical Society*, 333, 501
- Catelan P., Porciani C., 2001, *Monthly Notices of the Royal Astronomical Society*, 323, 713
- Chisari N. E., Dvorkin C., 2013, *Journal of Cosmology and Astroparticle Physics*, 12, 029
- DESI Collaboration 2024, in preparation
- DESI Collaboration 2025, in preparation
- DESI Collaboration et al., 2016b, The DESI Experiment Part I: Science, Targeting, and Survey Design, doi:10.48550/arXiv.1611.00036, <https://ui.adsabs.harvard.edu/abs/2016arXiv161100036D>
- DESI Collaboration et al., 2016a, The DESI Experiment Part II: Instrument Design, <https://ui.adsabs.harvard.edu/abs/2016arXiv161100037D>
- DESI Collaboration et al., 2022, *The Astronomical Journal*, 164, 207
- DESI Collaboration et al., 2023a, The Early Data Release of the Dark Energy Spectroscopic Instrument, doi:10.48550/arXiv.2306.06308, <https://ui.adsabs.harvard.edu/abs/2023arXiv230606308D>
- DESI Collaboration et al., 2023b, Validation of the Scientific Program for the Dark Energy Spectroscopic Instrument, doi:10.48550/arXiv.2306.06307, <https://ui.adsabs.harvard.edu/abs/2023arXiv230606307D>
- DESI Collaboration et al., 2024a, arXiv e-prints, p. arXiv:2404.03000
- DESI Collaboration et al., 2024b, arXiv e-prints, p. arXiv:2404.03001
- DESI Collaboration et al., 2024c, arXiv e-prints, p. arXiv:2404.03002
- Dark Energy Survey and Kilo-Degree Survey Collaboration et al., 2023, *The Open Journal of Astrophysics*, 6, 36
- Davis M., Efstathiou G., Frenk C. S., White S. D. M., 1985, *The Astrophysical Journal*, 292, 371
- Dey A., et al., 2019, *The Astronomical Journal*, 157, 168
- Eke V. R., et al., 2004, *Monthly Notices of the Royal Astronomical Society*, 348, 866
- Fortuna M. C., Hoekstra H., Joachimi B., Johnston H., Chisari N. E., Georgiou C., Mahony C., 2021, *Monthly Notices of the Royal Astronomical Society*, 501, 2983
- Galler B. A., Fisher M. J., 1964, *Commun. ACM*, 7, 301
- Georgiou C., et al., 2019, *Astronomy and Astrophysics*, 622, A90
- Georgiou C., van den Bosch F., van Dokkum P., Chardin N. E., 2023, *Desert Fishes and the Future of DESI: Impact on future surveys*, doi:10.48550/arXiv.2309.03841, <https://ui.adsabs.harvard.edu/abs/2023arXiv230903841>
- Guy J., et al., 2023, *The Astronomical Journal*, 165, 144
- Hadzhiyska B., Eisenstein D., Bose S., Garrison L. H., Maksimova N., 2021, *Monthly Notices of the Royal Astronomical Society*, 509, 501
- Hahn C., et al., 2023, *The Astronomical Journal*, 165, 253
- Hirata C. M., Seljak U., 2004, *Physical Review D*, 70, 063526
- Hirata C. M., Mandelbaum R., Ishak M., Seljak U., Nichol R., Pimbblet K. A., Ross N. P., Wake D., 2007, *Monthly Notices of the Royal Astronomical Society*, 381, 1197
- Joachimi B., et al., 2015, *Space Science Reviews*, 193, 1
- Krolewski A., et al., 2024, Impact and mitigation of spectroscopic systematics on DESI DR1 clustering measurements, doi:10.48550/arXiv.2405.17208, <https://ui.adsabs.harvard.edu/abs/2024arXiv240517208K>
- Kurita T., Takada M., 2023, *Physical Review D*, 108, 083533
- Lamman C., Tsaprazi E., Shi J., Niko Šarčević N., Pyne S., Legnani E., Ferreira T., 2023a, The IA Guide: A Breakdown of Intrinsic Alignment Formalisms, doi:10.48550/arXiv.2309.08605, <https://ui.adsabs.harvard.edu/abs/2023arXiv230908605L>
- Lamman C., et al., 2023b, *Monthly Notices of the Royal Astronomical Society*, 522, 117
- Lamman C., et al., 2024, *Monthly Notices of the Royal Astronomical Society*, 528, 6559
- Lasker J., et al., 2024, Production of Alternate Realizations of DESI Fiber Assignment for Unbiased Clustering Measurement in Data and Simulations, doi:10.48550/arXiv.2404.03006, <https://ui.adsabs.harvard.edu/abs/2024arXiv240403006L>
- Lee J., Ryu S., Baldi M., 2023, *The Astrophysical Journal*, 945, 15
- Levi M., et al., 2013, The DESI Experiment, a whitepaper for Snowmass 2013, doi:10.48550/arXiv.1308.0847, <https://ui.adsabs.harvard.edu/abs/2013arXiv1308.0847L>
- Maksimova N. A., Garrison L. H., Eisenstein D. J., Hadzhiyska B., Bose S., Satterthwaite T. P., 2021, *Monthly Notices of the Royal Astronomical Society*, 508, 4017
- Mena-Fernández J., et al., 2024, HOD-Dependent Systematics for Luminous Red Galaxies in the DESI 2024 BAO Analysis, doi:10.48550/arXiv.2404.03008, <https://ui.adsabs.harvard.edu/abs/2024arXiv240403008M>
- Miller T. N., et al., 2023, The Optical Corrector for the Dark Energy Spectroscopic Instrument, doi:10.48550/arXiv.2306.06310, <https://ui.adsabs.harvard.edu/abs/2023arXiv2306.06310>
- Myers A. D., et al., 2023, *The Astronomical Journal*, 165, 50
- Okuma T., 2019, *Physical Review D*, 100, 103507
- Okumura T., Taruya A., Nishimichi T., 2019, *Physical Review D*, 100, 103507
- Oppenheimer B. D., Babul A., Bahé Y., Butsky I. S., McCarthy I. G., 2021, *Universe*, 7, 209
- Philcox O. H. E., Slepian Z., Hou J., Warner C., Cahn R. N., Eisenstein D. J., 2022, *Monthly Notices of the Royal Astronomical Society*, 509, 2457
- Raichoor A., et al., 2023, *The Astronomical Journal*, 165, 126
- Robotham A. S. G., et al., 2011, *Monthly Notices of the Royal Astronomical Society*, 416, 2640
- Saga S., Shiraishi M., Akitsu K., Okumura T., 2024, *Physical Review D*, 109, 043520
- Schlafly E. F., et al., 2023, *The Astronomical Journal*, 166, 259
- Schneider M. D., Bridle S., 2010, *Monthly Notices of the Royal Astronomical Society*, 402, 2127
- Shi J., et al., 2024, *Monthly Notices of the Royal Astronomical Society*, 528, 1487
- Singh S., Mandelbaum R., 2016, *Monthly Notices of the Royal Astronomical Society*, 457, 2301
- Singh S., Mandelbaum R., More S., 2015, *Monthly Notices of the Royal Astronomical Society*, 450, 2195
- Slepian Z., Eisenstein D. J., 2015, *Monthly Notices of the Royal Astronomical Society*, 454, 4142
- Slepian Z., et al., 2017, *Monthly Notices of the Royal Astronomical Society*,

- 469, 1738
 Smargon A., Mandelbaum R., Bahcall N., Niederste-Ostholt M., 2012,
Monthly Notices of the Royal Astronomical Society, 423, 856
 Sunayama T., 2023, *Monthly Notices of the Royal Astronomical Society*, 521,
 5064
 Troxel M. A., Ishak M., 2015, *Physics Reports*, 558, 1
 Xu K., Jing Y. P., Zhao G.-B., Cuesta A. J., 2023, *Nature Astronomy*, 7, 1259
 Yuan S., Eisenstein D. J., Garrison L. H., 2017, *Monthly Notices of the Royal
 Astronomical Society*, 472, 577
 Yuan S., et al., 2024, *Monthly Notices of the Royal Astronomical Society*
 Zhou R., et al., 2023, *The Astronomical Journal*, 165, 58
 van Uitert E., Joachimi B., 2017, *Monthly Notices of the Royal Astronomical
 Society*, 468, 4502

Author Affiliations

- ¹Center for Astrophysics | Harvard & Smithsonian, 60 Garden Street,
 Cambridge, MA 02138, USA
²Departamento de Física, Universidad de los Andes, Cra. 1 No. 18A-
 10, Edificio Ip, CP 111711, Bogotá, Colombia
³Observatorio Astronómico, Universidad de los Andes, Cra. 1 No.
 18A-10, Edificio H, CP 111711 Bogotá, Colombia
⁴Lawrence Berkeley National Laboratory, 1 Cyclotron Road, Berkeley,
 CA 94720, USA
⁵Physics Dept., Boston University, 590 Commonwealth Avenue,
 Boston, MA 02215, USA
⁶Dipartimento di Fisica “Aldo Pontremoli”, Università degli Studi
 di Milano, Via Celoria 16, I-20133 Milano, Italy
⁷Department of Physics & Astronomy, University College London,
 Gower Street, London, WC1E 6BT, UK
⁸Instituto de Física, Universidad Nacional Autónoma de México, Cd.
 de México C.P. 04510, México
⁹University of California, Berkeley, 110 Sprout Hall #5800 Berkeley,
 CA 94720, USA
¹⁰Institut de Física d’Altes Energies (IFAE), The Barcelona Institute
 of Science and Technology, Campus UAB, 08193 Bellaterra
 Barcelona, Spain
¹¹Institut d’Estudis Espacials de Catalunya (IEEC), 08034
 Barcelona, Spain
¹²Institute of Cosmology and Gravitation, University of Portsmouth,
 Dennis Sciama Building, Portsmouth, PO1 3FX, UK
¹³Institute of Space Sciences, ICE-CSIC, Campus UAB, Carrer de
 Can Magrans s/n, 08913 Bellaterra, Barcelona, Spain
¹⁴Fermi National Accelerator Laboratory, PO Box 500, Batavia, IL
 60510, USA
¹⁵Center for Cosmology and AstroParticle Physics, The Ohio State
 University, 191 West Woodruff Avenue, Columbus, OH 43210, USA
¹⁶Department of Physics, The Ohio State University, 191 West
 Woodruff Avenue, Columbus, OH 43210, USA
¹⁷The Ohio State University, Columbus, 43210 OH, USA
¹⁸School of Mathematics and Physics, University of Queensland,
 4072, Australia
¹⁹Sorbonne Université, CNRS/IN2P3, Laboratoire de Physique Nucléaire et de Hautes Energies (LPNHE), FR-75005 Paris, France
²⁰NSF NOIRLab, 950 N. Cherry Ave., Tucson, AZ 85719, USA
²¹Institució Catalana de Recerca i Estudis Avançats, Passeig de Lluís
 Companys, 23, 08010 Barcelona, Spain
²²Department of Physics and Astronomy, Siena College, 515 Loudon
 Road, Loudonville, NY 12211, USA
²³Department of Physics & Astronomy and Pittsburgh Particle
 Physics, Astrophysics, and Cosmology Center (PITT PACC), University
 of Pittsburgh, 3941 O’Hara Street, Pittsburgh, PA 15260,

USA

²⁴Departamento de Física, Universidad de Guanajuato - DCI, C.P.
 37150, Leon, Guanajuato, México

²⁵Instituto Avanzado de Cosmología A. C., San Marcos 11 - Atenas
 202. Magdalena Contreras, 10720. Ciudad de México, México

²⁶Instituto de Astrofísica de Andalucía (CSIC), Glorieta de la As-
 tronomía, s/n, E-18008 Granada, Spain

²⁷Departament de Física, EEBE, Universitat Politècnica de
 Catalunya, c/Eduard Maristany 10, 08930 Barcelona, Spain

²⁸Department of Astronomy, The Ohio State University, 4055
 McPherson Laboratory, 140 W 18th Avenue, Columbus, OH 43210,
 USA

²⁹Department of Physics and Astronomy, Sejong University, Seoul,
 143-747, Korea

³⁰CIEMAT, Avenida Complutense 40, E-28040 Madrid, Spain

³¹Department of Physics, University of Michigan, Ann Arbor, MI
 48109, USA

³²University of Michigan, Ann Arbor, MI 48109, USA

³³National Astronomical Observatories, Chinese Academy of Sciences,
 A20 Datun Rd., Chaoyang District, Beijing, 100012, P.R.
 China

Many people made this work
 possible – this is just a list of
 the universities they’re from!

33 institutions,
 10 different countries



APPENDIX A: MODELLING DERIVATION

To compute the expectation value $\langle \epsilon \rangle$ between projected shapes and the 3D matter field, $\mathcal{E}_{\text{model}}$, we begin with their definitions, as described in Equation [\(A1\)](#).

$$\epsilon = \tau [T_{xx} - T_{yy} + 2iT_{xy}] \quad (\text{A1})$$

$$Q(R_{\text{bin}}, \pm\Pi_{\text{max}}) = \frac{\int d^3r W(\bar{r}) \delta e^{2i\theta_r}}{\int d^3r W(\bar{r})(1 + \xi_{\epsilon g})} \quad (\text{A2})$$

Using these, $\mathcal{E}_{\text{model}}$ is computed as:

$$\begin{aligned} \mathcal{E}_{\text{model}} &= \Re \langle \epsilon * Q \rangle = \frac{1}{2} \langle \epsilon^* Q + \epsilon Q^* \rangle = \Re \epsilon \Re Q + \Im \epsilon \Im Q = |Q| [(\epsilon_{xx} - \epsilon_{yy}) \cos 2\theta + 2\epsilon_{xy} \sin 2\theta] \\ &= \frac{-\tau}{\int d^3r W(\bar{r})(1 + \xi_{\epsilon g})} \int dz \int R dR \int d\theta W(\bar{r}) \delta(R, z) [(T_{xx} - T_{yy}) \cos 2\theta + (2T_{xy} - T_{xx} - T_{yy}) \sin 2\theta] \end{aligned} \quad (\text{A3})$$

The 3 dimensions we integrate over here are the projected angle on the plane of the sky θ , the projected distance R , and the redshift z . $*$ indicates complex conjugation and x^* is the complex conjugate of x . To compute the second integral, we convert to Fourier space.

$$\begin{aligned} \int dz \int R dR W(\bar{r}) \int d\theta \int \frac{d^3k}{(2\pi)^3} \tilde{\delta}(k) e^{-ik \cdot r} \int \frac{d^3q}{(2\pi)^3} e^{iq \cdot (0)} \tilde{\delta}q \frac{1}{q^2} [(q_x q_x - q_y q_y) \cos 2\theta + (2q_x q_y - q_x q_x - q_y q_y + \frac{2}{3}q^2) \sin 2\theta] \\ = \int dz \int R dR W(\bar{r}) \int \frac{dk_z}{2\pi} \int \frac{K dK}{(2\pi)^2} P(k) \int d\phi \int d\theta e^{-iK \cdot R - ik_z z} \frac{1}{k^2} \\ [K^2 (\cos^2 \phi - \sin^2 \phi) \cos 2\theta + K^2 (2 \cos \phi \sin \phi - (\cos^2 \phi + \sin^2 \phi)) \sin 2\theta + \frac{2}{3} k^2 \sin 2\theta] \end{aligned} \quad (\text{A4})$$

$\tilde{\delta}$ is the fractional overdensity in Fourier space. k represented the wavenumber in Fourier space, K represents the 2D position on the plane of the sky (k_x, k_y), and k_z along the line of sight. $k^2 = K^2 + k_z^2$. We use the 2D plane wave expansion $e^{iK \cdot R} = \sum_{n=-\infty}^{\infty} i^n J_n(KR) e^{in\psi}$, where $\cos \psi = \hat{K} \cdot \hat{R}$. The above expression will integrate to 0 for all n except $n = \pm 2$, allowing us to reduce $e^{iK \cdot R}$ to $-2J_2(KR)e^{2i(\theta-\phi)}$, of which the real component is $-2J_2(KR) \cos(2(\phi-\theta))$. The inner integrands becomes:

$$- \int_0^{2\pi} d\phi \int_0^{2\pi} d\theta 2J_2(KR) \cos 2(\phi-\theta) [K^2 \cos 2\theta + \frac{2}{3} (K^2 + k_z^2) \sin 2\theta] = -4\pi^2 J_2(KR) K^2 \quad (\text{A5})$$

This leads to our final expression,

$$\mathcal{E}_{\text{model}} = \frac{-\tau}{\int d^3r W(\bar{r})} \int dz \int R dR \int \frac{dk_z}{2\pi} \int \frac{K dK}{(2\pi)^2} P(k) \delta_{\text{model}}(R, z) \quad (\text{A6})$$

This is the fourth paper summary like this I've made!

This is solved numerically except for

For one on the discovery of dark energy, see [this link](#).

$$\mathcal{J}_2(K) = \frac{2}{(R_{\text{max}}^2 - R_{\text{min}}^2) \int R dR} \int \frac{dk_z}{2\pi} \int \frac{K dK}{(2\pi)^2} P(k) \delta_{\text{model}}(R, z) \quad (\text{A7})$$

for which we use the analytic solution:

$$\mathcal{J}_2(K, R) = \frac{2}{(R_{\text{max}}^2 - R_{\text{min}}^2) K^2} [2J_0(KR_{\text{min}}) + KR_{\text{min}} J_1(KR_{\text{min}}) - 2J_0(KR_{\text{max}}) - KR_{\text{max}} J_1(KR_{\text{max}})] \quad (\text{A8})$$

This paper has been typeset from a [TeX/LaTeX](#) file prepared by the author.

If you've gotten this far, CONGRATULATIONS!
I hope my notes made it easier to digest this
paper. If you're a scientist, I would love to
read similar notes on one of your papers :)
- Claire Lamman

I made this in power point using the XKCD font:
<https://github.com/ipython/xkcd-font>

